Structural and Multidisciplinary Optimization (2025) 68:5
https://doi.org/10.1007/s00158-024-03936-2

RESEARCH PAPER

A geometry projection method for topology optimization of frames with structural shapes

Nicolás Cuevas-Carvajal[1] · Miguel F. Montoya-Vallejo[2] · Julián A. Norato[1]

Received: 5 April 2024 / Revised: 11 September 2024 / Accepted: 7 November 2024

Abstract
We present a topology optimization method based on the geometry projection technique for the design of frames made of structural shapes. An equivalent-section approach is formulated that represents the cross-section of the structural shapes as a homogeneous rectangular section. The accuracy of this approach is demonstrated by comparison to analyses performed using body-fitted meshes of the original sections for different loads and boundary conditions. A novel geometric representation is also introduced to represent the equivalent section as a cuboid. Like offset solids, this representation is endowed with an explicit expression for the computation of the signed distance to the boundary of the primitive and of its sensitivities, allowing for an efficient implementation. An overlap constraint is imposed via the formulation of auxiliary primitives associated to the structural members, which guarantees the resulting designs do not exhibit impractical intersections of primitives that would preclude their construction. The efficacy and efficiency of the method is demonstrated via 2D and 3D design examples. The examples demonstrate that the proposed method renders optimal designs and exhibits good convergence. They also illustrate the ability to design structures with far lower optimal volume fractions than those typically employed in continuum topology optimization techniques.

Keywords Feature mapping · Structural shapes · Structural profiles · Ultralight frame structures · Equivalent section

1 Introduction

Structural shapes (also known as structural profiles) are widely used in structural design, including in aerospace, automotive, and civil engineering structures. Their extensive use owes to the standardization of dimensions and mechanical properties, making them readily available, practical, reliable, and easy to economically assemble. Common applications of these structures include machinery frames; civil structures like roofs, bridges, domes, and buildings; frames for aerospace applications like instruments and satellites; support structures for power transmission and chemical processing plants; and offshore platforms, to mention a few. Structural shapes have been used for more than a century (Bates and Association 1987) and therefore robust and mature technologies exist for their design, simulation, and fabrication. Although prescribed solutions that are well-understood and easy to fabricate exist for particular applications (e.g., bridges), there are frame design problems (for instance, those with irregularly shaped design regions) for which it is not intuitive to determine optimal frame designs, therefore we must resort to structural design techniques such as topology optimization.

The first topology optimization techniques used for the design of frame structures made of stock elements are the so-called ground-structure methods (cf. Zegard and Paulino 2014; Rozvany 2011; Bendsøe 2004). In these methods, the stock members are modeled using 1D finite elements, such as truss and beam elements. A ground structure is created whereby a predefined set of nodes in the structure are connected among each other using 1D elements. The optimization consists of modifying the size of each element, i.e., the cross-sectional area, with a zero size for a

Communicated by Seonho Cho.

✉ Nicolás Cuevas-Carvajal
nicolas.cuevas_carvajal@uconn.edu

[1] School of Mechanical, Aerospace, and Manufacturing Engineering, University of Connecticut, 191 Auditorium Road, U3139, Storrs, Connecticut 06269, USA

[2] Ingeniería Mecánica, Escuela Colombiana de Ingeniería Julio Garavito, AK. 45 No. 205 - 59, Autopista Norte, Bogotá 111166, Colombia

Published online: 24 December 2024

member indicating it should be removed from the design. Some techniques also optimize the spatial positions of the nodes of the ground structure (Bendsøe et al. 1994). These methods have the advantage of being computationally efficient, since the analysis with 1D elements is inexpensive. Moreover, they readily accommodate using structural shapes like the ones considered in this work by assigning the corresponding section properties to the beam or truss elements. However, these techniques have two important limitations: the topology of the optimal design is restricted to a subset of the ground structure, which may significantly decrease the design freedom; and the 1D representation cannot capture multi-dimensional stress states and so it cannot model stress concentrations arising at the joints due to intersections of the structural elements. Although the present work does not consider stress requirements, this is an important consideration that the authors wish to address in future work, which precludes the use of ground-structure methods. In light of these limitations, we focus on topology optimization techniques for continua.

Conventional density-based and level-set methods for continuum topology optimization (cf. Sigmund and Maute 2013) cannot in general be used to design this type of structures, as they render organic designs that cannot be easily realized with structural shapes. An alternative to design frame structures with structural shapes using topology optimization for continua is feature-mapping techniques (Wein et al. 2020). In these methods, the structure is represented via the combination of geometric primitives such as bars and plates. These primitives are described by high-level parameters associated with their dimensions, size and orientation. To perform the analysis, this parameterization is mapped onto, for example, a density field that facilitates the analysis on a fixed mesh in the same manner as density-based methods. While feature-mapping methods have been used successfully to design structures made of solid bars and plates, they are yet to be used for design with structural shapes. The reason for this shortcoming is that these techniques require a finite element size small enough to accurately capture the structural behavior of each bar, and to ensure design sensitivities are well defined (Norato et al. 2015; Zhang et al. 2016). Roughly speaking, at least two elements are required through the thickness of the primitive. In the case of structural shapes, having two elements through the thickness of, e.g., the webs and flange of an H-beam or the wall of a tube would result in a large number of elements that would make the finite element analysis expensive and impractical. For example, consider the design of a bridge with a design space of 10 m $\times$ 3 m $\times$ 2 m and using an H-beam IPE 220 section. For this profile, the web thickness t_w and flange thickness t_f are 5.9 mm and 9.2 mm, respectively. Capturing the structural behavior of these elements with reasonable accuracy would require a mesh with an element size of at least than 5.9/2 mm = 2.95 mm. This would result in a mesh of more than 2.3 billion elements, which is clearly unrealistically large for the purpose of designing the bridge. For this reason, while feature-mapping techniques have been used to model structural shapes such as rectangular tubes (Bai and Zuo 2020; Zhao et al. 2021; Wang et al. 2024), the dimensions of the design region are comparable to those of the structural shapes, and the volume fraction of the optimal structure is much larger ($\geq 20\%$) than that of the structures considered in this work ($\leq 2\%$). It should also be noted that some methods have modeled panel stiffeners with structural shapes by employing beam elements to model the stiffeners, and planar elements (e.g., shells) (Li et al. 2019; Savine et al. 2021) or a meshless discretization (Li et al. 2021) to model the panel to be reinforced. However, these methods do not obtain optimal three-dimensional frames made of structural shapes that are not connected to a panel but only to each other.

To address these shortcomings, this work formulates a topology optimization method based on the geometry projection technique for the design of frames made of structural shapes. An equivalent-section approach is formulated that represents the cross-section of the structural shapes as a homogeneous rectangular section. The accuracy of this approach is demonstrated by comparison to analyses performed using body-fitted meshes of the original sections for different loads and boundary conditions. A novel geometric representation is also introduced to represent the equivalent section as a cuboid. Like the offset solids typically used in geometry projection techniques, this representation is endowed with an explicit expression for the computation of the signed distance to the boundary of the primitive and of its sensitivities, allowing for an efficient implementation. An overlap constraint is imposed via the formulation of auxiliary primitives associated to the structural members, which guarantees the resulting designs do not exhibit impractical intersections of primitives that would preclude their construction.

The remainder of the paper is structured as follows. Section 2 presents the formulation and validation of the equivalent-section methodology. Section 3 introduces the geometry projection method, which constitutes the basis of the method developed in this work. A novel geometric representation of these equivalent sections is subsequently formulated in Sect. 4. The optimization problem description is detailed in Sect. 5. Examples of the application of the proposed technique to two design problems are detailed in Sect. 6. Finally, Sect. 7 presents the conclusions of this work.

2 Equivalent section of structural shapes

As noted in Sect. 1, the central idea of the proposed work is to replace the intricate cross-sections of structural shapes with a solid rectangular (in 2D) or cuboid or cylindrical (in 3D) section of equivalent bending and axial stiffness. The advantage of doing this, is that the equivalent solid section can be meshed with much larger elements than what would be needed to mesh the structural shape, providing substantial computational savings. The proposed procedure is similar to the standard treatment given in mechanics of materials to composite beams (Hibbeler and Yap 2022) made of multiple materials.

In this work we consider H-beam, square-tube and cylindrical-tube structural shapes. We find an equivalent rectangular section in 2D and an equivalent cuboid section in 3D for all shapes. For the tubular section, a circular equivalent section could also be considered, but we do not consider it here for ease of implementation.

2.1 Determination of dimensions and modulus of equivalent section

The equivalent-section methodology starts from the consideration that the original and equivalent beams must have the same axial deformation under axial loading. To ensure equivalency of the bending deformation, we start by considering the Euler-Bernoulli equation for beam deflection

$$EI\frac{\mathrm{d}^4u}{\mathrm{d}x^4} - p = 0, \tag{1}$$

where u denotes the beam deflection, p is the applied vertical load by unit length, E is the modulus of elasticity, and I is the second moment of area. Since the real and equivalent beams must have the same solution $u(x)$, it can be readily concluded that $E_0I_0 = E_eI_e$, where the subscripts 0 and e denote the original and equivalent properties, respectively. Note that E_0 corresponds to the modulus E of the actual material the shape is made of, but we add the sub-index for clarity to differentiate it from the equivalent modulus E_e. Equation (1) must be satisfied for any orientation of the cross-section area, i.e., the Mohr's circle of the inertia scaled by E has to be the same for the original and equivalent sections. Therefore, equivalent properties for any cross-section need only be computed for its principal axes. In the case of the sections considered in this work, the principal axes correspond to the symmetry axes. For original cross-sections that are not symmetric (e.g., C-channels), one need simply consider asymmetric equivalent sections (i.e., they can be rectangular but with an off-center bending axis).

The second relationship considered is the differential equation for axial strain of a bar made of a linearly elastic material, given by

$$\frac{\mathrm{d}}{\mathrm{d}x}\left(AE\frac{\mathrm{d}\delta}{\mathrm{d}x}\right) + T = 0, \tag{2}$$

where δ is the axial deformation, T is the axial load, and A the cross-section area. As before, the axial deformation of the original and equivalent beams should be the same, which is ensured when $E_0A_0 = E_eA_e$. It should be noted that both original and equivalent beams are assumed to have the same length. The previous considerations can be summarized in the following system equations:

$$\begin{aligned} E_0{I_0}^w &= E_e{I_e}^w \\ E_0{I_0}^s &= E_e{I_e}^s \\ E_0A_0 &= E_eA_e. \end{aligned} \tag{3}$$

The superscripts w and s denote the weak and strong axes of the section, respectively. We consider an equivalent rectangular section of dimensions $2a \times 2b$. For 2D-problems, we assume the section's strong and weak axes lie in-plane and out-of-plane, respectively, and the analysis is performed considering plane-stress conditions. Note that we use a rectangular section not only for the H-beam and square-tube shapes, but also for the circular tube, since the plane-stress analysis assumes a uniform out-of-plane thickness of the 2D-elements. For 3D-problems, the rectangular section corresponds to a cuboid-shaped primitive. For this rectangular section, the equivalent modulus E_e and dimensions a and b can be easily obtained from (3) as

$$\begin{aligned} E_0{I_0}^w &= E_e\frac{4ba^3}{3} \\ E_0{I_0}^s &= E_e\frac{4b^3a}{3} \\ E_0A_0 &= E_e4ab. \end{aligned} \tag{4}$$

Note that since the foregoing derivation of equivalent modulus and dimensions is based on the Euler beam equation (1), the equivalency is valid only under the conditions for which the Euler beam theory is valid, namely, that: a) the material is homogeneous, which is automatically satisfied by assuming a single modulus E_e for the equivalent section; b) the undeformed beam is straight, which is satisfied by the geometric representation of the beams used in the proposed method and described in Sect. 4; and c) that the cross-section remains flat under deformation. The latter requirement is satisfied by imposing a minimum length for the beams, just like in Euler beam theory (see, for example, Öchsner 2021), as demonstrated in Sect. 2.2.

It should also be noted that the polar moment of inertia J_e of the equivalent section satisfies

$E_eJ_e = E_eI_e^w + E_eI_e^s = E_0I_0^w + E_0I_0^s = E_0J_0$. This relation is independent of the coordinate system, since $I_0^w + I_0^s$ is the trace of the area moment of inertia tensor, which is an invariant. Therefore, even though the polar moment of inertia should not be used for non-circular cross-sections that may experience out-of-plane warping, it is reasonable to assume the original and equivalent sections have similar torsional rigidity.

2.2 Numerical validation

To validate that the equivalent sections provide a reasonably accurate approximation of the bending and axial deformation of beams made of structural shapes, we perform a comparison of finite element analyses of beams made of the original structural shape and of the equivalent section. We consider three structural shapes (see Fig. 1): an IPE 220 H-beam with dimensions $t_f = 9.2$ mm, $t_w = 5.9$ mm, $b_f = 110$ mm, and $d = 220$mm; an RHS rectangular tube with dimensions $b_f = 120$ mm, $d = 200$ mm, and $t_f = 8$ mm; and a CHS circular tube of diameter $d = 219.1$ mm and $t_f = 5$ mm.

Table 1 shows the cross-section properties of the original section, and the dimensions, modulus and cross-sectional properties of the respective equivalent section obtained from (4).

Two types of problems are considered, depicted in Fig. 2: a cantilever beam and a simply supported beam. Five independent loads are applied to the cantilever beam: concentrated bending loads F_X, F_Y and an axial load F_Z applied at the tip, and distributed loads W_X and W_Y uniformly applied along the beam's length. Four independent loads are applied to the simply supported beam: concentrated bending loads F_X and F_Y applied at the center point, and distributed loads W_X and W_Y uniformly applied along the beam's length.

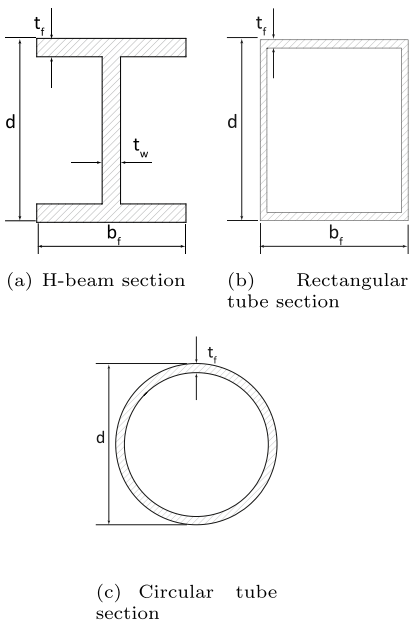

(a) H-beam section (b) Rectangular tube section

(c) Circular tube section

Fig. 1 Structural shapes considered in this work

Table 1 Cross-section properties of the original and respective equivalent sections

	H-section	Rectangular tube	Circular tube
Shape	IPE 220	RHS 200x120 / 8	CHS 219.1 / 5
A_0(mm^2)	3213.44	4864.00	3363.07
$I_0{}^s$(×10^6 mm^4)	26.53	26.01	19.28
$I_0{}^w$(×10^6 mm^4)	2.04	11.55	19.28
E_0(GPa)	200	200	200
a(mm)	157.37	126.66	131.15
b(mm)	43.69	84.41	131.15
E_e(GPa)	23.370	22.747	9.777
A_e(×10^3 mm^2)	27.50	42.77	68.80
$I_e{}^s$(×10^6 mm^4)	227.02	228.70	394.40
$I_e{}^w$(×10^6 mm^4)	17.49	101.57	394.40

The beams are modeled with hexahedral elements. For beams made of the equivalent section, a 3D model made of hexahedral elements is considered. Finite element models for beams of different lengths are created, and the corresponding linear elastic analyses performed. The analyses are performed with the commercial software ANSYS Static Structural. The effectiveness of the equivalent-section approach is determined by computing the relative error of the y-displacement u_y at the center point of the cross-section, measured at the tip of the cantilever beam and the center point (along z-direction) of the simply supported beam:

$$e_r = \frac{|u_{y_e} - u_{y_r}|}{u_{y_r}}. \tag{5}$$

For tubular-shape sections, which are hollow and thus have no finite element node at the center point of the cross-section, we simply add a shell mesh with negligible thickness at the z-position where the displacement is measured (i.e.,

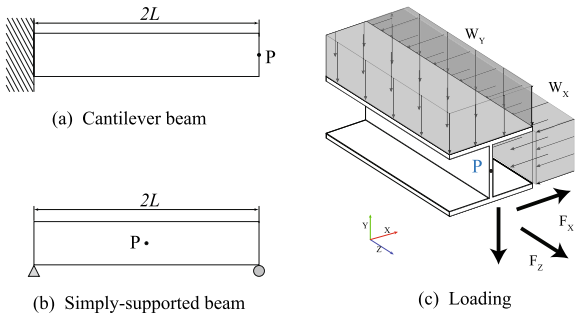

(a) Cantilever beam (b) Simply-supported beam (c) Loading

Fig. 2 Boundary conditions and loading cases considered in the validation

at the tip for the cantilever beam, and at the center for the simply supported beam).

Figure 3 shows the displacement error of (5) for the H-section as a function of the ratio L/d of the length of the beam to its characteristic dimension. Figures for the rectangular-tube and circular-tube shapes are not shown for brevity, but the results are similar. All sections present a monotonic decrease of the error with increasing beam length. The error for short beams is large, and this is expected since the assumptions of Euler beam theory are no longer valid. For beams with $L/d \geq 10$, the relative error is at most 3%, which we deem to be sufficiently accurate for the optimization. Therefore, in the proposed optimization technique, we will consequently impose a constraint that $L/d \geq 10$ for all beams.

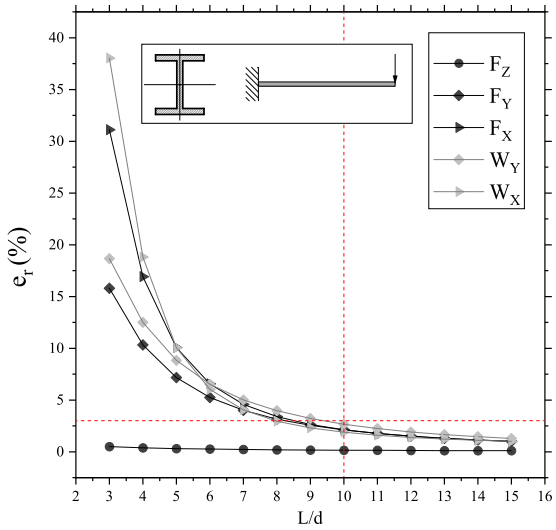

(a) Cantilever beam

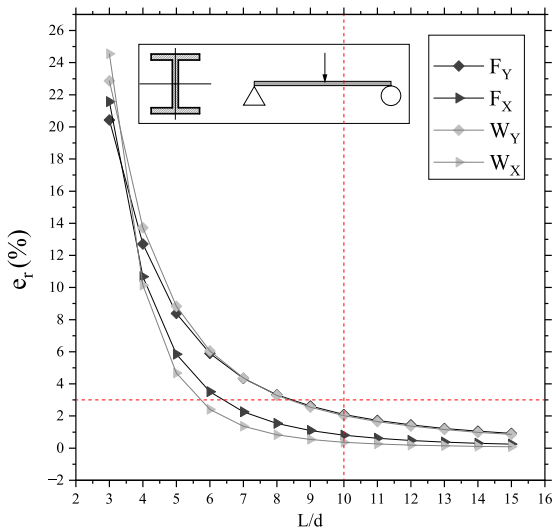

(b) Simply supported beam

Fig. 3 Relative displacement error for H-beam with rectangular equivalent section

3 Geometry projection

To map the geometric primitives representing the equivalent shapes onto the finite element mesh for analysis, we use the geometry projection method (Norato et al. 2015; Zhang et al. 2016). A projected density is computed as

$$\rho_c\left(\frac{\phi_c(\mathbf{p},\mathbf{z}_c)}{r}\right) := \begin{cases} 0, & \text{if } \phi_c/r < -1 \\ \widetilde{H}(\phi_c/r), & \text{if } -1 \leq \phi_c/r \leq 1 \\ 1, & \text{if } \phi_c/r > 1 \end{cases}, \quad (6)$$

where $\mathbf{z}_c$ denotes the vector of design parameters for primitive c, ϕ_c is the signed distance to the boundary $\partial\omega_c$ of primitive c, r is a sampling radius, and

$$\widetilde{H}(x) = \begin{cases} 1 - \frac{\arccos x + x\sqrt{1-x^2}}{\pi}, & \text{in 2D} \\ \frac{1}{2} + \frac{3x}{4} - \frac{x^3}{4}, & \text{in 3D.} \end{cases} \quad (7)$$

is a differentiable approximation of the Heaviside function. Although the projected density can be computed at any point in space, an element-wise projected density is computed at the centroid of each element. The radius r of the sample window is typically chosen relative to the element size (for instance, equal to the element largest diagonal), and it is fixed throughout the optimization.

An important and unique aspect of geometry projection methods is the introduction of a membership variable $\alpha_c \in [0, 1]$. This variable, as in solid isotropic material penalization (SIMP) techniques used in density-based topology optimization, is penalized so that a value of 0.0 indicates the primitive must be removed altogether from the design regardless its dimensions and position, whereas a value of 1.0 indicates the primitive must be retained in the design. The membership variable is used to define an *effective density* at element e as

$$\widehat{\rho}_{ce}(x, z_c, q) := \mu(\alpha_c\, \rho_c, q), \quad (8)$$

where μ is a penalization function and q is the penalization parameter. For example, for SIMP penalization, $\mu(x, q) = x^q$. The effect of this membership variable is that it makes it easier for the optimizer to remove a primitive and avoid falling in poor local minima. Moreover, the use of the membership variables often leads to better convergence behavior.

To consider a structure made of multiple primitives, they are combined via a Boolean union. When the representation of the primitives is implicit, as is the case for the signed distance function, the Boolean union corresponds to the maximum of the signed distance functions for all primitives

(Shapiro 2002). Since the maximum function is not differentiable and we wish to employ efficient gradient-based optimization methods, we replace the maximum function with a differentiable approximation. Here, we consider the *softmax* approximation introduced by Smith and Norato (2021) that computes the effective elasticity tensor for element e as the linear combination

$$\mathbb{C}_e = \mathbb{C}_{\text{void}} + \sum_{c}^{n_c} \beta(c, \hat{\boldsymbol{\rho}}_e, p)\, \widehat{\rho}_{ce}(\mathbb{C}_c - \mathbb{C}_{\text{void}}), \tag{9}$$

where $\mathbb{C}_c$ is the elasticity tensor for the material that primitive c is made of, $\mathbb{C}_{\text{void}}$ is the elasticity tensor of a weak material to ensure a well-posed analysis, n_c is the number of primitives, and $\hat{\boldsymbol{\rho}}_e \in \mathbb{R}^{n_c}$ is the vector of effective densities ρ_{ce} for element e. The weights of the softmax linear combination with parameter p are given by

$$\beta(i, \mathbf{x}, p) := \underset{i}{\text{softargmax}}(i, \mathbf{x}, p) = \frac{e^{px_i}}{\sum_j e^{px_j}}. \tag{10}$$

Note that the values of $\beta(c, \hat{\boldsymbol{\rho}}_e, p)$ for all primitives form a one-hot vector, with a component value ≈ 1.0 corresponding to the largest value of $\widehat{\rho}_{ce}$ of any primitive c, and ≈ 0.0 for all other vector components. Therefore, a point in the design region is effectively assigned the elasticity tensor of at most one of the available primitives. An advantage of this combination scheme over previous expressions used in geometry projection methods (e.g., those used in Norato et al. 2015; Zhang et al. 2016) is that it easily accommodates situations where the primitives are made of different and/or anisotropic materials. Finally, the volume of the structure is computed as

$$V = \sum_e \check{\rho}_e v_e, \tag{11}$$

where v_e is the volume of element e and

$$\check{\rho}(\mathbf{x}) = \sum_{c}^{n_c} \beta(c, \hat{\boldsymbol{\rho}}_e, p)\, \widehat{\rho}_{ce} \tag{12}$$

is a combined density. Note that an advantage of the softmax approximation as compared to other differentiable approximations of the maximum is that it renders a combined density strictly in the range [0, 1].

The computation of design sensitivities of a function J with respect to a geometric parameter z_i in geometry projection techniques simply requires a chain rule:

$$\frac{DJ}{dz_i} = \sum_e^{n_e} \frac{\partial J}{\partial \rho_e} \frac{\partial \rho_e}{\partial z_i} + \frac{DJ}{dz_i}, \tag{13}$$

where DJ/dz_i denotes the total derivative, $\partial J/\partial \rho_e$ is computed as in density-based methods (without penalization), and $\partial \rho_e/\partial z_i$ can be computed from the geometry projection.

4 Geometric representation of equivalent sections

The offset bars commonly used in geometry projection techniques (cf. Norato et al. 2015; Smith and Norato 2020 do not accommodate the rectangular and cuboid equivalent sections detailed in Sect. 2 because they are circular cylinders with semispherical ends. This chapter introduces a novel geometric representation for the equivalent section shapes. The computation of the signed distance for the proposed representation differs from that of offset solids, for which it simply corresponds to subtracting the radius (or thickness) r_b of the offset solid from the distance d_{be} to the medial axis (or surface) of the primitive.

The representation proposed in this work corresponds to a cuboid with rounded edges. The boundary of the primitive is partitioned in multiple regions. A coordinate transformation follows, which allows a ready identification of the closest-surface region, after which a straightforward distance calculation to that region is made. Therefore, as with offset solids, the computation of the signed distance and its design sensitivities can be efficiently made in closed form as a function of the design parameters, which precludes the need for iterative techniques to compute the signed distance (as in, e.g., Norato 2018).

The rounded corners and edges in 2D and 3D, respectively, ensure the signed distance field is differentiable everywhere and consequently renders a robust behavior with gradient-based optimization techniques. Although the proposed representation is formulated for rectangular and cuboid regions, the region subdivision strategy can be generalized to polygonal (or polytope) shapes. While other feature-mapping methods have considered such representations (see, for instance, Chandrasekhar (2023); Zhang and Zhou (2018)), these representations employ sharp corners and edges, which lead to non-differentiability of the signed distance.

4.1 Definition of the primitives

For rectangular equivalent sections, we propose a representation with rounded corners like the one shown in Fig. 4. Although the rounded corners ensure the distance function is differentiable at points along the diagonals of the rectangle, it should be noted that the distance function is always non-differentiable at points on the medial axis. A local coordinate system $(x', y', z')_c$ is associated with the rectangular cross-section of primitive c, with the x' and y' axes aligned with the sides of dimensions a and b, respectively, and the z' axis perpendicular to the plane of the section. The dimensions, position, and orientation of the bar c with rectangular equivalent section are

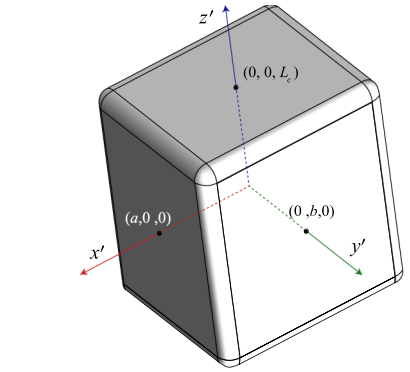

(a) Primitive representation

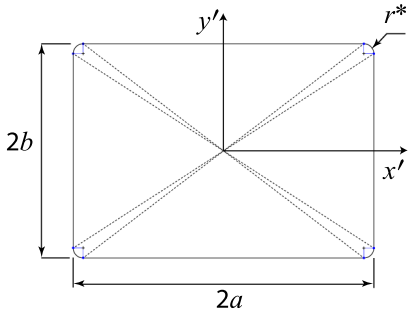

(b) Cross-section of the primitive for $z' = 0$

Fig. 4 Primitive representation

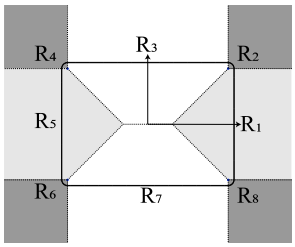

(a) 2D

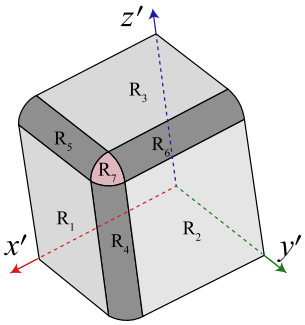

(b) 3D

Fig. 5 Regions used to compute the signed distance field

$\{a, b, L_c, \mathbf{q}_c, \mathbf{t}_c, r^*\}$, where $\mathbf{q}_c = \{q_0, q_1, q_2, q_3\}_c$ is the vector of quaternions that determines the primitive's orientation, and $\mathbf{t} = \{t_x, t_y, t_z\}_c$ is the position of the center of the primitive in the global coordinate system. The orientation of the primitives via quaternions is detailed in Sect. 4.4.

The transformation of a point $\mathbf{p}'$ from the local primitive coordinate system to the global coordinate system is given by

$$\mathbf{p} = \mathbf{R}(\hat{\mathbf{q}}_c)\mathbf{p}' + \mathbf{t}_c, \tag{14}$$

where $\mathbf{R}$ is the rotation matrix given by (21). Conversely, the global-to-local system transformation is given by

$$\mathbf{p}' = \mathbf{R}^T(\hat{\mathbf{q}}_c)(\mathbf{p} - \mathbf{t}_c), \tag{15}$$

where we use the fact that $\mathbf{R}$ is a rotation matrix and therefore orthogonal, hence its inverse equals its transpose.

4.2 Signed distance field computation

The computation of the signed distance for the proposed rectangular equivalent section rests on the fact that the distance in Euclidean space is rotation-invariant with respect to the coordinate system. Figure 5 illustrates the concept of the signed distance computation for the proposed representation using a 2D-representation only. To compute the distance from a point $\mathbf{p}$ to the primitive c, we first transform $\mathbf{p} \rightarrow \mathbf{p}'$ to the local coordinate system $(x', y', z')_c$ of the primitive using (15). Using the components of $\mathbf{p}'$, it is then simple to determine in the local coordinate system which of the eight regions of the primitive shown in Fig. 5 contains the closest point to $\mathbf{p}'$, and a simple expression renders the signed distance. We can make an additional simplification to this procedure by taking advantage of the fact that the proposed section is symmetric with respect to the x'-z' and y'-z' planes: we first reflect the point so that it always lies on the first quadrant of x'-y':

$$\tilde{\mathbf{p}}' = |\mathbf{p}'|. \tag{16}$$

Consequently, we only need to check $\tilde{\mathbf{p}}'$ for Regions 1–3, see Table 2.

For 2D design problems, for which we employ a plane-stress assumption in the analysis and consequently employ a rectangular equivalent section, it is assumed the weak axis of the beam is out of plane. Also, in 2D it is easier to directly work with a single orientation angle θ_c instead of the two quaternions. With these considerations, the vector of five design variables for bar c in the case of 2D-problems is given by $\mathbf{z}_c^{2D} = \{L_c, \theta_c, t_{x_c}, t_{y_c}, \alpha_c\}$; the out-of-plane thickness of the plane elements used for the analysis is set to b; L_c corresponds to the in-plane length of the bars; and the in-plane-width of the bars is fixed and set to a. It should be noted that this geometric representation

Table 2 Signed distance for rectangular region in 2D. $\Delta x := a - r^* - \tilde{p}'_x$; $\Delta y := L_c - r^* - \tilde{p}'_y$

Region	Definition	$\phi_c(\tilde{\mathbf{p}}', \mathbf{z}_c)$
1	$(\Delta y \leq \Delta x) \wedge (0 \leq \Delta y)$	$\Delta x + r^*$
2	$(0 > \Delta x) \wedge (0 > \Delta y)$	$r^* - \sqrt{\Delta x^2 + \Delta y^2}$
3	$(\Delta y > \Delta x) \wedge (0 < \Delta x)$	$\Delta y + r^*$

allows for the optimization of structures made of structural profiles with arbitrary cross-sections (for example, an H-beam) as a solid bar in 2D. The vector of nine design variables for bar c in the case of 3D-problems is given by $\mathbf{z}_c^{3D} = \{L_c, q_{0_c}, q_{1_c}, q_{2_c}, q_{3_c}, t_{x_c}, t_{y_c}, t_{z_c}, \alpha_c\}$. As before, a and b are fixed.

For the 3D-bars with rectangular cross-section proposed in this work (see Fig. 5(b)), we use a similar strategy to subdivide the space in regions. The cuboid has three planes of symmetry and so, as before, we obtain the reflection $\tilde{\mathbf{p}}'$ of $\mathbf{p}'$ that lies on the first quadrant $(x', y', z' \geq 0)$, and then use the components of $\tilde{\mathbf{p}}'$ to determine which of the seven regions shown in Fig. 5(b) it belongs to; an appropriate expression is subsequently used to compute the signed distance, see Table 3.

It should be noted that the equivalent cross-section dimensions a and b are non-designable in the optimization, since they are chosen to provide the equivalent properties of the structural profiles, as described in Sect. 2. All remainder parameters describing the dimensions, position, and orientation of the bars are designable. That is, the vector of design variables for bar c is given by $\mathbf{z}_c = \{L_c, \mathbf{q}_c, \mathbf{t}_c, \alpha_c\}$, where we recall that α_c is the bar's membership variable. This amounts to five design variables in 2D (with one angle and two components of the translation vector), and nine design variables in 3D. The edges' rounding radius r^* is fixed and chosen as much smaller than the bar's cross-section dimensions. Note that having L_c as a design variable allows the easy imposition of the minimum length requirement described in Sect. 2.2, as it can be prescribed as a lower bound on the variable.

4.3 Sensitivities of the signed distance

To enable the use of efficient gradient-based non-linear programming methods for the optimization, it is necessary to compute design sensitivities of the objective and constraints of the optimization problem. As noted in Sect. 3, this requires a chain-rule computation, for which the design sensitivities of the signed distance are required. As seen from the expressions listed in Tables 2–3, the signed distance has both an explicit dependence on the bar's dimensions a, b, and L_c, and an implicit dependence on the bar's quaternions $\mathbf{q}_c$ and translation vector $\mathbf{t}_c$ through the transformation (15). Therefore, the signed-distance sensitivities with respect to the design variable z_i are computed as

$$\frac{D\phi}{dz_i} = \frac{\partial \phi}{\partial \tilde{\mathbf{p}}'}^T \frac{D\tilde{\mathbf{p}}'}{d\mathbf{p}'} \frac{D\mathbf{p}'}{dz_i} + \frac{\partial \phi}{\partial z_i} \tag{17}$$

with

$$\frac{D\mathbf{p}'}{dz_i} = \frac{D\mathbf{R}}{dz_i}^T (\mathbf{p} - \mathbf{t}_c) - \mathbf{R}^T \frac{D\mathbf{t}_c}{dz_i}, \tag{18}$$

which we obtain by differentiating (15), and

$$\frac{D\tilde{\mathbf{p}}'}{d\mathbf{p}'} = \text{diag}(\text{sgn}(\mathbf{p}')), \tag{19}$$

which we obtain by differentiating (16). Clearly, $D\mathbf{R}/dz_i = 0$ for any design variable other than the bar's quaternions. The derivatives of $\mathbf{R}$ with respect to the quaternions can be obtained by differentiation of (21)–(23). The term $D\mathbf{t}_c/dz_i = 1$ when z_i corresponds to one of the components of $\mathbf{t}_c$, and it is zero otherwise. The terms $\partial\phi_c/\partial\tilde{\mathbf{p}}'$ and $\partial\phi_c/\partial z_i$ can be readily derived from Tables 2 and 3 for 2D- and 3D-problems, respectively.

An important observation is that it can be readily shown that the expressions for the signed distance are the same at the points/edges between the regions. For example, it can be seen in Table 2 that when $\tilde{y}' = b - r^*$, the expression for the signed distance of Region 2 simplifies to $a - \tilde{p}'_x$, which is the same expression for Region 1; and when $\tilde{x}' = a - r^*$, the expression

Table 3 Signed distance for cuboid region in 3D. $\Delta x := a - r^* - \tilde{p}'_x$; $\Delta y := b - r^* - \tilde{p}'_y$; $\Delta z := L_c - r^* - \tilde{p}'_z$

Region	Definition	$\phi_c(\tilde{\mathbf{p}}', \mathbf{z}_c)$
1	$(\Delta x \leq \Delta y) \wedge (\Delta y \leq \Delta z) \wedge (0 < \Delta y) \wedge (0 < \Delta z)$	$\Delta x + r^*$
2	$(\Delta x > \Delta y) \wedge (\Delta y \leq \Delta z) \wedge (0 < \Delta x) \wedge (0 < \Delta z)$	$\Delta y + r^*$
3	$(\Delta x > \Delta z) \wedge (\Delta y > \Delta z) \wedge (0 < \Delta x) \wedge (0 < \Delta y)$	$\Delta z + r^*$
4	$(0 \geq \Delta x) \wedge (0 \geq \Delta y) \wedge (0 < \Delta z)$	$r^* - \sqrt{\Delta x^2 + \Delta y^2}$
5	$(0 \geq \Delta x) \wedge (0 < \Delta y) \wedge (0 \geq \Delta z)$	$r^* - \sqrt{\Delta x^2 + \Delta z^2}$
6	$(0 < \Delta x) \wedge (0 \geq \Delta y) \wedge (0 \geq \Delta z)$	$r^* - \sqrt{\Delta y^2 + \Delta z^2}$
7	$(0 \geq \Delta x) \wedge (0 \geq \Delta y) \wedge (0 \geq \Delta z)$	$r^* - \sqrt{\Delta x^2 + \Delta y^2 + \Delta z^2}$

for the signed distance of Region 2 simplifies to $b - \tilde{p}'_y$, which is the same expression for Region 3. This is expected, as the bar is a regular solid and the signed distance must be continuous. However, importantly, the signed-distance derivatives are also continuous at the shared points/edges. Again for Table 2, for example, $\partial\phi/\partial a = 1$ and $\partial\phi/\partial b = 0$ when $\tilde{y}' = b - r^*$ for both Region 1 and Region 2. It can be verified that all other design derivatives (i.e., with respect to the quaternions and translation vector components) are also the same. This shows that the rounded corners ensure continuity of the design sensitivities of the signed distance, which leads to robustness of the gradient-based optimization.

4.4 Primitives orientation via quaternions

In addition to specifying the primitive's dimensions and position, the orientation of the primitives must also be stipulated. Early geometry projection techniques for topology optimization with plates (e.g., Zhang et al. 2016) employed Euler angles to describe the primitive's orientation. However, as noted in Smith and Norato (2022b), this description of the orientation can lead to a gimbal-lock-type of situation where one design of freedom is lost, making it more difficult for the optimizer to progress towards a good design. To circumvent this problem, Smith and Norato (2022b) introduced the use of quaternions to define the orientation of the primitive.

A quaternion is an extension of the concept of complex number, with one real and three imaginary parts. The property of interest of these numbers (specifically, of unit quaternions) is their ability to represent orientation in a 3D space (Kuipers 2020). The parameterization of the orientation of a primitive with quaternions has the advantage over an Euler-angles representation that it does not suffer from gimbal lock. Moreover, rotations of the primitive and design derivatives of these rotations can be easily computed.

The quaternion for primitive c is given by $\mathbf{q}_c = \{q_0, q_1, q_2, q_3\}_c \in \mathbb{R}^4$. Euler's rotation theorem states that any rotation of a rigid body or coordinate system can be represented by a single rotation θ about an axis $\mathbf{a}$ called the Euler axis. The quaternion is related to this rotation as

$$\mathbf{q} = \{\cos(\theta/2), a_1 \sin(\theta/2), a_2 \sin(\theta/2), a_3 \sin(\theta/2)\}. \quad (20)$$

The rotation matrix associated with the unit quaternion $\hat{\mathbf{q}}$ is given by

$$\mathbf{R}_{3D} = \begin{bmatrix} 1 - 2\hat{q}_2^2 - 2\hat{q}_3^2 & 2\hat{q}_1\hat{q}_2 - 2\hat{q}_0\hat{q}_3 & 2\hat{q}_1\hat{q}_3 + 2\hat{q}_0\hat{q}_2 \\ 2\hat{q}_1\hat{q}_2 + 2\hat{q}_0\hat{q}_3 & 1 - 2\hat{q}_1^2 - 2\hat{q}_3^2 & 2\hat{q}_2\hat{q}_3 - 2\hat{q}_0\hat{q}_1 \\ 2\hat{q}_1\hat{q}_3 - 2\hat{q}_0\hat{q}_2 & 2\hat{q}_2\hat{q}_3 + 2\hat{q}_0\hat{q}_1 & 1 - 2\hat{q}_1^2 - 2\hat{q}_2^2 \end{bmatrix} \quad (21)$$

for 3-dimensional rotations, with

$$\hat{\mathbf{q}} = \frac{\mathbf{q}}{\|\mathbf{q}\|}. \quad (22)$$

For rotations in the $\mathbf{e}_1 - \mathbf{e}_2$ plane about the $\mathbf{e}_3$ axis, $q_1 = q_2 = 0$. Using the half-angle formulas together with (20) and (22), it can be readily shown that (21) simplifies to the well known rotation matrix

$$\mathbf{R}_{2D} = \begin{bmatrix} \cos\theta & \sin\theta & 0 \\ -\sin\theta & \cos\theta & 0 \\ 0 & 0 & 1 \end{bmatrix}. \quad (23)$$

5 Optimization problem

The optimization problem considered in this work is that of minimizing the structural compliance subject to a constraint on the amount of material. While consideration for other structural criteria is obviously necessary for structural design, it is outside of the scope of this work and deferred to future work. The minimum-compliance problem is stated as

$$\begin{aligned} &\min_{\mathbf{z}} \mathcal{J}(\mathbf{z}) := \log(\mathcal{C}(\mathbf{z}) + 1) \\ &\text{subject to:} \\ &\mathbf{K}(\mathbf{z})\mathbf{u}(\mathbf{z}) = \mathbf{f} \\ &v(\mathbf{z}) \le \bar{v}_{eq} \\ &g_{\text{cont}}(\mathbf{z}) \le \epsilon_{\text{cont}} \\ &g_{\text{over}}(\mathbf{z}) \le 1 \\ &\underline{z}_i \le z_i \le \bar{z}_i, \forall z_i \in \{\mathbf{z}\}, \end{aligned} \quad (24)$$

where $\mathbf{z} = \{\mathbf{z}_1, \cdots, \mathbf{z}_{n_c}\}$ is the vector of design variables for the n_c bars, with $\mathbf{z}_c$ the vector of design variables for bar c as described in Sect. 4.2; also,

$$\mathcal{C}(\mathbf{z}) = \mathbf{u}^\top(\mathbf{z})\mathbf{f} \quad (25)$$

is the structural compliance, $\mathbf{u}$ is the displacement vector, $\mathbf{f}$ is the design-independent force vector, and $\mathbf{K}$ is the global stiffness matrix. The logarithmic form of the objective function, which was introduced in Smith and Norato (2022a), exhibits better convergence behavior than the compliance itself and is adopted in this work.

The volume fraction of the structure relative to the design region is denoted by v, and it is defined as

$$v(\mathbf{z}) := \frac{V(\mathbf{z})}{\sum_e v_e}, \quad (26)$$

where V is the volume of the structure given by (11) and we recall v_e is the element volume. It is important to note that

the volume fraction computed via (26) corresponds to the equivalent section. Therefore, if a particular volume fraction limit $\bar{v}$ is desired for the actual original section, an equivalent limit $\bar{v}_{eq}$ must be used for the optimization. This can be simply computed as

$$\bar{v}_{eq} = \frac{A_{eq}}{A_0}\bar{v}. \tag{27}$$

The constraints g_{cont} and g_{over} in (24), detailed in the sequel, ensure the bars remain fully contained within the design region, and that bars do not overlap in undesired ways, respectively.

As in previous geometry projection techniques (cf. Norato et al. 2015), the design variables are scaled to improve convergence and to enable the imposition of a uniform move limit for all design variables:

$$\hat{z}_i = \frac{z_i - \underline{z}_i}{\overline{z}_i - \underline{z}_i}, \tag{28}$$

where $\underline{z}_i$ and $\overline{z}_i$ denote the lower and upper bounds of design variable z_i, respectively. A move limit m is imposed on the design variables at iteration I to prevent large, erratic design steps in the optimization:

$$\max\left(0, \hat{z}_i^{(I-1)} - m\right) \leq \hat{z}_i^{(I)} \leq \min\left(1, \hat{z}_i^{(I-1)} + m\right). \tag{29}$$

The optimization is stopped after any of the following three criteria are satisfied: 1) the relative change of the objective function in two consecutive iterations does not exceed a specified threshold, i.e., $|\mathcal{J}^{(I)} - \mathcal{J}^{(I-1)}|/\mathcal{J}^{(I)} \leq \epsilon_{\mathcal{J}}$; 2) the maximum relative change of any design variable in two consecutive iterations does not exceed a specified threshold, i.e., $\|\mathbf{z}^{(I)} - \mathbf{z}^{(I-1)}\|_\infty \leq \epsilon_z$; or 3) the iteration reaches a maximum number of iterations $\max_{\text{iter}}$.

5.1 Containment constraint

One important practical consideration is to ensure that primitives are fully contained within the design region. If a portion of a primitive lies outside the design region, it has no effect on the analysis and should be removed in the physical realization of the structure. This could lead to cuts of the primitives that are highly impractical (for instance, a cut at a small angle relative to the long axis of the bar). Moreover, a bar that lies partially outside the design region and is therefore cut in the fabrication could end up violating the minimum length constraint. For these reasons, it is desirable to ensure that the bars lie completely within the design region.

One way to enforce this requirement is by using the so-called ghost-points technique (Zhang et al. 2018), whereby a set of ghost points is created just outside the boundaries of the design region. A constraint is introduced in the optimization that a differentiable approximation of the maximum combined density of (12) at these points is smaller than a specified value $0 < \epsilon_n \ll 1$. In other words, the combined density of any ghost point must be near zero. While this method is effective and has the advantage of being independent of the geometric representation used for the primitives, here we adopt the simpler approach introduced in Kazemi et al. (2020), whereby we force the difference between the volume of a primitive computed via the geometry projection (i.e., (11), here denoted as V_{num_c}) and that computed directly from the primitive's geometric parameters (here denoted as V_{geom_c}) to be negligible. We define a volume difference ratio as

$$\xi_c = \left(\frac{V_{\text{geom}_c} - V_{\text{num}_c}}{V_{\text{geom}_c}}\right)^2. \tag{30}$$

If a primitive c is entirely contained in the design space, ξ_c should be close to zero. It is desirable to define a single constraint for all of the primitives, as otherwise we would have as many constraints as primitives, which makes it increasingly difficult for non-linear programming methods to incorporate in the optimization. To this end, we employ the lower-bound Kreisselmeier-Steinhauser (LKS) function as a differentiable approximation of the maximum volume difference ratio of all primitives, and define the *containment* function as

$$g_{\text{cont}}(\mathbf{z}) = \underset{c}{LKS}\left(\xi_c(\mathbf{z}_c)\right), \tag{31}$$

with

$$\underset{i}{LKS}(\mathbf{x}) := \frac{1}{k}\ln\left(\frac{1}{n}\sum_i e^{kx_i}\right), \mathbf{x} \in \mathbb{R}^n, \tag{32}$$

where k is a parameter such that as $k \to \infty$, $LKS(\mathbf{x}) \to \max(\mathbf{x})$.

5.2 Overlap constraint

A second aspect that must be addressed for practical purposes is the overlap of primitives. There is nothing preventing the optimizer from placing primitives such that they overlap so as to obtain a larger structural member. For example, the optimizer may place one primitive right on top of another so that the effective load path provides, e.g., larger bending stiffness. While this is numerically correct, it is impractical from a fabrication and assembly point of view. We therefore wish to avoid these overlaps. This problem was addressed previously in Smith and Norato (2019) for offset

bars with circular ends, whereby a no-overlap constraint limits only allows the ends of the bars to be connected to other bars. That is, it is possible for the end regions of a bar to be connected to any portion of another bar; but overlaps between the middle portion of two bars are precluded.

The approach formulated in this work is in the same spirit as the constraint of Smith and Norato (2019), but it avoids the need for Boolean operations by using an auxiliary primitive associated to each bar. These auxiliary primitives are defined by introducing two positive parameters $f_L < 1$ and $f_a > 1$. For 2D-bars with dimensions $a \times L_c$ the dimensions of the corresponding auxiliary primitive are $f_a a \times f_L L_c$, see Fig. 6(a). The idea of the proposed overlap constraint is that the sum of the projected densities corresponding to all the auxiliary primitives at any point in the design region should not exceed 1.0. This means that two auxiliary primitives cannot overlap. cf. Fig. 6(b). On the other hand, overlaps between the regions of each bar outside of the auxiliary primitives with any region of another bar are permitted, cf. Fig. 6(c). The overlap constraint can be similarly formulated for 3D-bars by defining an auxiliary primitive with dimensions $f_a a_c \times f_a b \times f_L L_c$.

As with the containment constraint, we wish to apply a single constraint for all the elements in the mesh. We therefore use again the LKS function and define the overlap constraint as

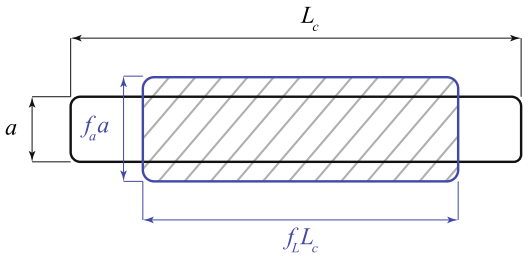

(a) Auxiliary primitive dimensions

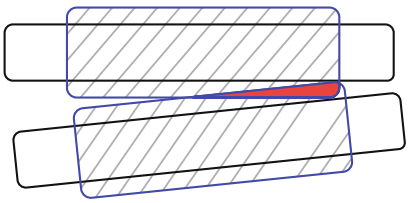

(b) Example of a forbidden overlap

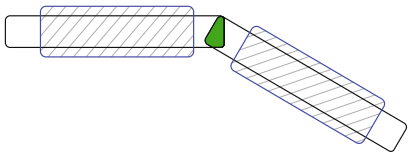

(c) Example of an allowed overlap

Fig. 6 Auxiliary primitives for overlap constraint

$$g_{over}(\mathbf{z}) = \underset{e}{LKS}\left(\sum_c \alpha_c^{\eta(1-\alpha_c)} \rho_{ce}^*\right), \tag{33}$$

where ρ_{ce}^* is the projected density of the auxiliary primitive of the bar c at the centroid of element e. This projected density is computed via (6) and using the signed distance corresponding to the dimensions of the auxiliary primitive.

The purpose of the term $\alpha_c^{\eta(1-\alpha)}$ is to make sure that components with low membership variables are not counted in the sum. A continuation strategy is used for this term and controlled by the parameter η. For $\eta > 0$, there is a range $\alpha \in [0, \bar{\eta}]$ for which this term is close to zero. The larger the value of η, the larger $\bar{\eta}$. At the beginning of the optimization, η is set to a value of, e.g., $\eta_0 = 6$. For this value, for example, $\alpha_c^{\eta(1-\alpha_c)} < 10^{-3}$ for $\alpha_c \in [0, 0.225]$. This means that bars with membership variable values less than 0.225 are effectively not counted in the overlap constraint, which allows for more overlaps in the initial optimization iterations. The parameter η is subsequently decreased every time the relative change in the objective function at iteration I relative to the previous iteration falls below a specified value, i.e., when $|\mathcal{J}^{(I)} - \mathcal{J}^{(I-1)}|/|\mathcal{J}^{(I-1)}| < \epsilon_\eta$. The decrease is given by

$$\eta \leftarrow \max(\eta_{\min}, \eta - \Delta\eta). \tag{34}$$

As η decreases, $\bar{\eta}$ decreases and low-membership variable variables are penalized further, until overlaps are completely penalized for $\eta \approx 0$.

It should be noted that we are applying the overlap constraint using the bars with the equivalent sections. Since the equivalent sections are larger than the original ones, a design with the equivalent sections that satisfies the overlap constraints will guarantee there will be no overlaps with the original sections. However, it is possible that there is a better design with the original sections than the optimal design obtained with the equivalent sections (i.e., with lower value of $\mathcal{J}$), such that the equivalent-section representation of that design presents overlaps.

It is worth noting this overlap constraint is not straightforward to implement in ground-structure methods that use 1D elements for the analysis, (cf. Changizi and Jalalpour 2017)), since it is not trivial to compute intersections of the bars at arbitrary orientations and positions based on their geometric representations. It is also not straightforward to implement such an overlap constraint in feature-mapping methods that combine the geometric components prior to mapping the geometric representation onto the analysis mesh (the so-called combine-then-map strategies in Wein et al. (2020)), since once the components have been combined into a single representation, it is not possible to easily determined where they intersect.

The optimization problem is solved using the method of moving asymptotes (MMA) of Svanberg (1987). The

MMA parameters used to perform the optimization are presented in Table 4 for completeness and to ensure replicability of our results; the reader is referred to the foregoing reference for a detailed explanation of these parameters. As in Guest et al. (2011); Norato et al. (2022), we modify the parameter `asyinit` in MMA to produce a more conservative approximation of the optimization functions in the first two optimization iterations.

The computation of the sensitivities of the compliance and volume fraction is the same as that presented in, for example, Norato et al. (2015); Smith and Norato (2020). The only difference is that the derivatives of the signed distance for the proposed geometric representation in this work are those of Sect. 4.3 as opposed to those of an offset bar presented in those works. The sensitivities of the overlap constraint can be readily obtained by differentiation of (33), which in turn requires the derivatives of the projected density of (6) and the signed distance of Sect. 4.3.

A flowchart showing the high-level steps of the proposed method is shown in Fig. 7

Table 4 Optimization parameters. Note E_{void} and ν_{void} are the elastic modulus and the Poisson constant, respectively, that define the elasticity tensor of the void material $\mathbb{C}_{\text{void}}$ in (9)

Property	Value	Reference
q	3	(8)
m	0.05	(29)
$\max_{\text{iter}}$	300	Sect. 5
ϵ_{cont}	0.002	(31)
k_{LKS}	8	(31)
k_{LKS}	8	(33)
ϵ_{η}^{2D}	0.0004	(34)
ϵ_{η}^{3D}	0.0005	(34)
$\eta_{\min}$	0.1	(34)
$\Delta\eta$	1	(34)
η_0	6	(34)
r^*(mm)	25	Tables 2, 3
E_{void}	10^{-4}	(9)
ν_{void}	0.33	(9)
a_0	1	MMA
a_1	0	MMA
c_1	1000	MMA
d_1	1	MMA
`asyinit`	0.1	MMA

6 Results

This section presents examples of the implementation of the proposed method to solve the minimal-compliance topology optimization problem formulated in Sect. 2. Every example is solved using an H-beam (IPE 220), a rectangular tube (RHS 200 × 120 / 8) and a cylindrical tube (CHS 219.1 / 5). The beams are all made of steel, with properties shown in Table 1. To make the examples comparable, equivalent volume fraction limits $\bar{v}_{eq}$ are computed for each of these sections so that the real volume fraction limit $\bar{v}$ is the same for all designs. Three examples are presented: the well-known 2D Messerschmitt-Bölkow-Blohm (MBB) beam, a 2D bridge, and a 3D bridge. A plane-stress condition is assumed for the 2D models. Table 4 lists the values of all method parameters used. For the finite element analysis, we use square and cubic elements in 2D and 3D, respectively, whose size h is chosen so that $h \geq \min(a, b)$, which, as discussed in Sect. 1, is necessary to ensure continuous sensitivities. All problems are solved using a workstation with an AMD Rysen 9 7950X3D 16-Core Processor, base clock speed of 4.2 GHz, an NVIDIA GeForce RTX 4090 (24 GB) card, and 64GB of RAM.

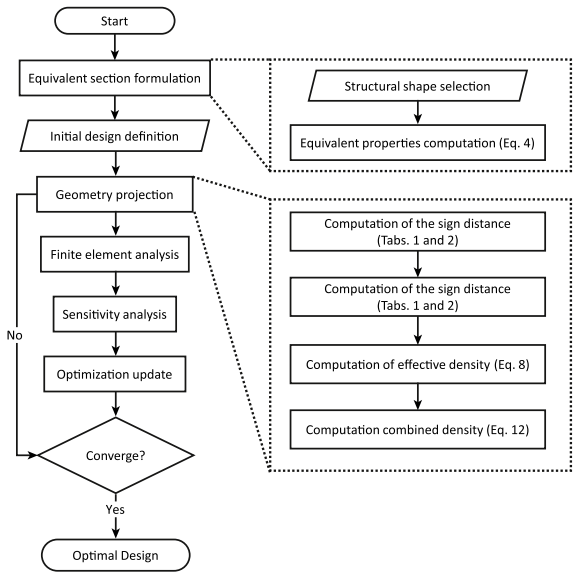

Fig. 7 Flowchart of the optimization process

6.1 2D MBB-beam

Only half of the MBB-beam is modeled using symmetry boundary conditions on the right edge, as shown in Fig. 8. A real volume fraction limit of steel $\bar{v}$ of 3% is imposed on the design.

Sensitivities for all of the functions in problem (24) are verified against finite-difference sensitivities. For this problem, we use the values f_a=1.7 and f_L=0.65 for the overlap constraint, and $\epsilon_{\mathcal{J}} = 8 \times 10^{-6}$ and $\epsilon_z = 4 \times 10^{-3}$ for the stopping criteria.

To exemplify the progression from the initial to the optimal design, Fig. 9 shows some intermediate designs during the optimization for the structure obtained with a circular tube. The initial design, composed of 25 disconnected bars, is shown in Fig. 9(a). The lengths L_c of all bars in the initial

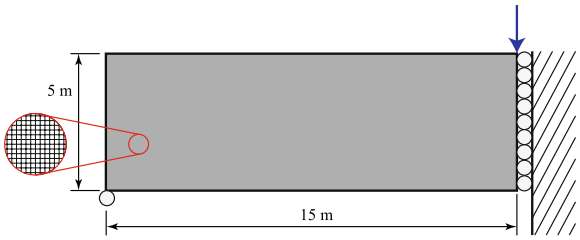

Fig. 8 Dimensions, loading, and boundary conditions for MBB-beam problem

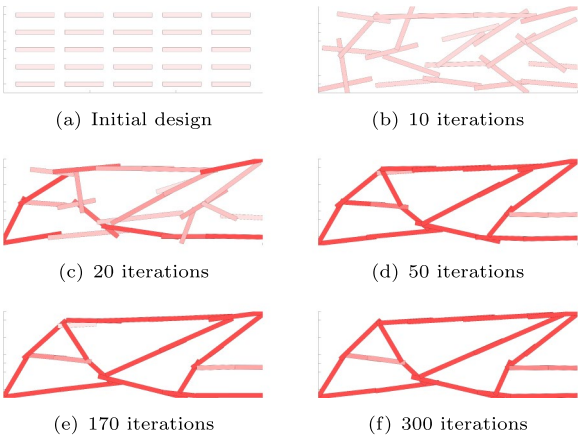

Fig. 9 Design iterates for MBB-beam optimization with circular-tube section. In this and subsequent 2D-design plots, the transparency of the color of the bars is proportional to the penalized membership variable α_c^q

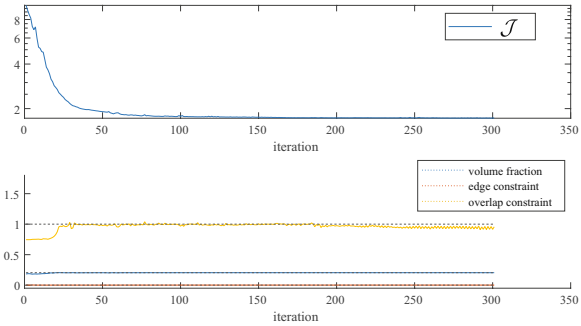

Fig. 10 Optimization function history for MBB-beam optimization with circular-tube section. The dotted lines denote the constraint limits

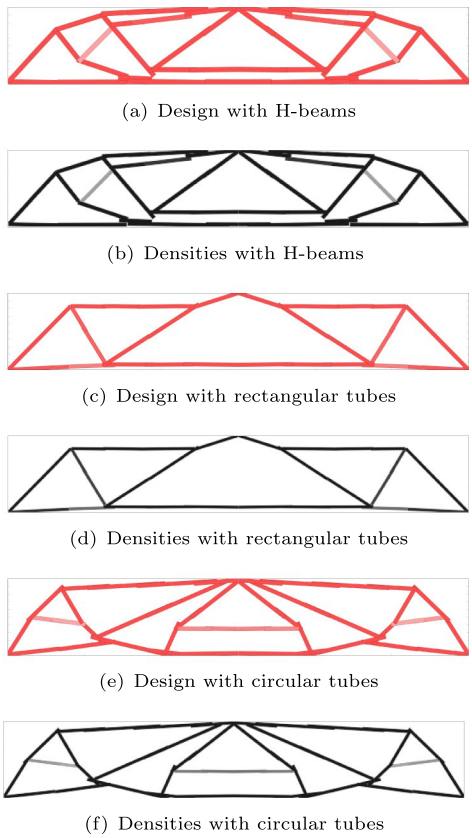

Fig. 11 MBB-beam optimization for the three different structural sections considered. The optimal design and density field are reflected about the symmetry line to show the entire beam. In this and subsequent figures, the plotted density corresponds to the combined density of (12)

design are set to satisfy the minimum length condition ($L/d \geq 10$) discussed in Sect. 2. The history of the objective and constraint functions for this circular-tube MBB-beam design shown in Fig. 10 indicates the method exhibits good convergence and feasibility of the design. This behavior was observed in all the examples presented in this work.

The optimal MBB-beam designs for all three sections are shown in Fig. 11 along with their corresponding combined density plots. Table 5 presents information related to each section, including: the dimensions $2a \times 2b$ of the equivalent cross-section; the bounds on the design variables L_c, θ_c, t_x, t_y, and α; the number of elements $n_x \times n_y$ in each dimension; the corresponding total number of elements in the mesh N_e; the number of iterations to convergence N_{ite}; and the equivalent volume fraction $\bar{v}_{eq}$, the average wall-clock time per iteration t_{ite}, the total wall-clock time t_{total} for the entire optimization; and the compliance $\mathcal{C}$ of the optimal designs.

It is observed that, as expected, the optimal designs for all three sections look different. For instance, as can be seen in Table 5, the optimal design obtained with the rectangular tube performs the worst, and the H-beam performs the best (i.e., they have the highest and lowest compliance, respectively). This is as we would expect, since the applied loading is in-plane, and the H-beam and rectangular tube offer the highest and lowest in-plane inertia-to-volume ratio, respectively; that is, the ratio I_0^s/A_0 is highest for the H-beam and lowest for the rectangular tube (cf. Table 1). This is reflected in the fact that the

Table 5 Summary of the MMB-beam optimization data for $\bar{v} = 3\%$

MBB-beam optimization			
Property	H-beam	Rectangular tube	Circular tube
$r *_c$(mm)	25	25	25
a(mm)	157.371	126.661	131.145
$2 * b$(mm)	87.374	168.820	262.29
L_c	[1100,7500]	[1000,7500]	[1100,7500]
θ_c	$[-2\pi, 2\pi]$	$[-2\pi, 2\pi]$	$[-2\pi, 2\pi]$
t_x(mm)	[0,15000]	[0,15000]	[0,15000]
t_y(mm)	[0,5000]	[0,5000]	[0,5000]
α	[0,1]	[0,1]	[0,1]
$\bar{v}_{eq}$	25.67%	13.65%	20.44%
N_e	24300	24300	24300
$n_x \times n_y$	270×90	270×90	270×90
N_{ite}	237	285	300
t_{ite} (s)	2.43	2.00	2.19
t_{total} (s)	582.74	576.35	664.73
$\mathcal{C}$ (J)	2102.32	2690.66	2584.24

dimension a of the equivalent section is largest for the H-beam and lowest for the rectangular tube (cf. Table 1); and that the equivalent volume fraction is largest for the H-beam and lowest for the rectangular tube (cf. Table 5).

It should be noted that in the maximum stiffness design of structures subject to a single load condition, the optimal design should be made of tension-compression members aligned with the principal strains, as long as the constraints on the geometry allow it (see, for example, Bendsøe and Haber (1993)). Therefore, the bending stiffness of the structural shape (and of the equivalent section) is irrelevant, and what dictates the design is the axial stiffness of the members. Consequently, if the cross-sections of two types of structural shapes have the same area but different area moments of inertia, the optimal designs will be similar. The reason we get different designs in the examples presented in this section is the difference in the cross-sectional areas of the shapes and, to a smaller extent, the overlap constraint; this is because even if the cross-sectional areas of the shapes are the same, their area moments of inertia —and hence the dimensions of their equivalent sections and of the auxiliary regions for the overlap constraint—are different.

The optimal design with the circular-tube section is compared with a conventional structural analysis using 1D beam elements, carried out in ANSYS Structural (see Fig. 12). The location of the center points of the bars, their length and their orientation in the optimal design are used to create geometric line bodies in ANSYS. Since the bars in the proposed method are represented as solids, their corresponding line bodies do not intersect. Therefore, these lines are subsequently extended or trimmed as necessary to ensure

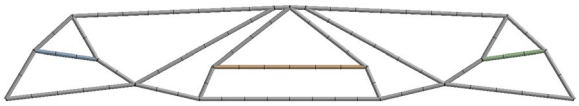

Fig. 12 ANSYS comparison with optimal design

the frame is connected. These line bodies are meshed with ANSYS, which generates multiple beam elements along each line body (corresponding to the segments that can be observed in Fig. 12). BEAM188 ANSYS elements are used, which are based on Timoshenko theory and are the default 2-node beam elements in ANSYS. It should be noted that ANSYS uses a 3-dimensional representation of the beam elements for visualization (i.e., the one shown in Fig. 12, however they are 1-dimensional elements. The elastic modulus of the elements that have an intermediate membership variable in the optimal design (i.e., those that appear 'gray' in Fig. 11(f)) is computed in ANSYS as $\alpha^q * E_0$, to account for the penalization of the density field.

An absolute error of 11% is found between the compliance of the density-based and the ANSYS model. This error can be attributed to multiple factors, including the fact that some bars have intermediate values of the membership variable and the different degrees of accuracy of the two models. Another important source of error will likely be the modeling of member intersections. The 1D model does not capture correctly the 2D- and 3D-intersections between bars, because bars are modeled as a line segment. The geometry projection technique, on the other hand, does capture multi-dimensional intersections; however, it also incurs in error in the modeling of these intersections because the dimensions of the equivalent sections are larger than those of the original section. Nevertheless, we deem this difference to be reasonable for conceptual design purposes.

6.2 2D bridge

This section presents 2D- and 3D-bridge design examples to demonstrate the proposed methodology on a common structural design problem. Considering the symmetry of the problem, a 2D topology optimization problem is first solved for half of the design region with symmetry boundary conditions (shown in blue in Fig. 13(a)). It is assumed the deck is supported through its length by a non-designable horizontal beam, represented as a fixed primitive in the topology optimization. A uniform distributed loading is applied on this beam; and a zero-displacement boundary condition is applied over a portion of the left edge of the design volume (shown in red in Fig. 13(a)). This fixed support is chosen to be disconnected from the horizontal beam so that the stiffness of the bridge comes primarily from the designable structure. The initial design for all runs, consisting of 20

bars, is shown in Fig. 13(b). For this problem, we use the values f_a=1.5 and f_L=0.65 for the overlap constraint, and $\varepsilon_{\mathcal{J}} = 1 \times 10^{-7}$ and $\varepsilon_z = 2 \times 10^{-3}$ for the stopping criteria.

The optimal 2D-bridge designs for all three sections are shown in Fig. 14 along with their corresponding combined density plots for $\bar{v} = 2\%$. Table 6 presents information related to each section. In this case, the best results are found with the H-beam, as expected. The design obtained with the rectangular tube renders a poor (i.e., high) compliance value. We posit the optimizer reaches this poor local minimum because of the relatively low equivalent volume fraction for this type of beam. Finally, the membership variables for some of the bars in the circular-tube design are relatively low and may be artificially increasing the compliance. If those bars are removed, the compliance would increase noticeably; or, if they are made fully solid, the volume fraction would increase noticeably.

6.3 3D bridge

The dimensions of the 3D-bridge are shown in Fig. 15. Symmetry boundary conditions are employed so that only a quarter of the design region is modeled; the symmetry planes are marked with a blue hashing in Fig. 15. As in the 2D bridge, a non-designable primitive is used to represent the deck, on which a uniform loading is applied. Zero-displacement boundary conditions are imposed on the region, shown with a red hashing in Fig. 15. For this problem, we use the values f_a=1.7 and f_L=0.75 for the overlap constraint, and $\varepsilon_{\mathcal{J}} = 1 \times 10^{-4}$ and $\varepsilon_z = 4 \times 10^{-3}$ for the stopping criteria.

Figure 16 shows some intermediate designs produced by the optimization for the design obtained with a circular tube to illustrate the evolution from the initial to the optimal design. The initial design for all runs is shown in Fig. 16(a), and it is again composed of 20 bars.

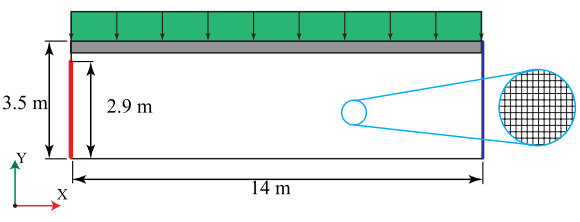

(a) Design space and boundary conditions

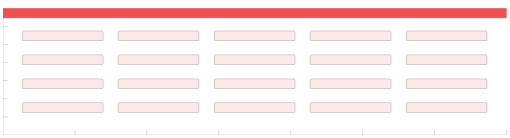

(b) Initial design

Fig. 13 Configuration of the 2D-bridge example

(a) Design with H-beams

(b) Densities with H-beams

(c) Design with rectangular tubes

(d) Densities with rectangular tubes

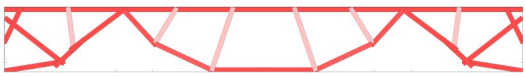

(e) Design with circular tubes

(f) Densities with circular tubes

Fig. 14 2D-bridge optimization for the three different structural sections considered. The optimal design and density field are reflected about the symmetry line to show the entire bridge

The optimal 3D-bridge designs for all three sections with $\bar{v} = 0.2\%$ are shown in Fig. 17. Table 7 presents information related to each section for the 3D problem including the bounds on the design variables L_c, q_0, q_1,

Table 6 Summary of the 2D-bridge optimization for 2% of steel

2D bridge beam optimization			
Property	H-beam	Rectangular tube	Circular tube
$r*_c$(mm)	25	25	25
a(mm)	157.371	126.661	131.145
$2*b$(mm)	87.374	168.820	262.29
L_c(mm)	[1100,7500]	[1000,7500]	[1100,7500]
θ_c	$[-2\pi, 2\pi]$	$[-2\pi, 2\pi]$	$[-2\pi, 2\pi]$
t_x(mm)	[0,14000]	[0,14000]	[0,14000]
t_y(mm)	[0,3500]	[0,3500]	[0,3500]
α	[0,1]	[0,1]	[0,1]
$\bar{v}_{eq}$	25.67%	13.65%	20.44%
N_e	12544	12544	12544
$n_x \times n_y$	224×56	224×56	224×56
N_{ite}	161	254	300
t_{ite} (s)	1.17	1.00	1.15
t_{total} (s)	193.70	259.82	351.12
$\mathcal{C}$ (J)	2601.68	4333.63	2681.72

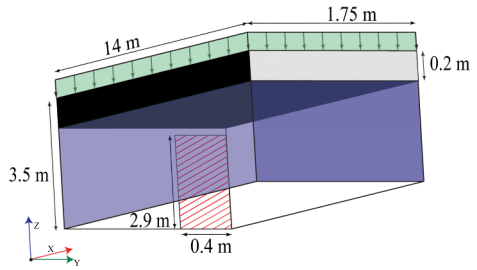

Fig. 15 Design space for 3D bridge

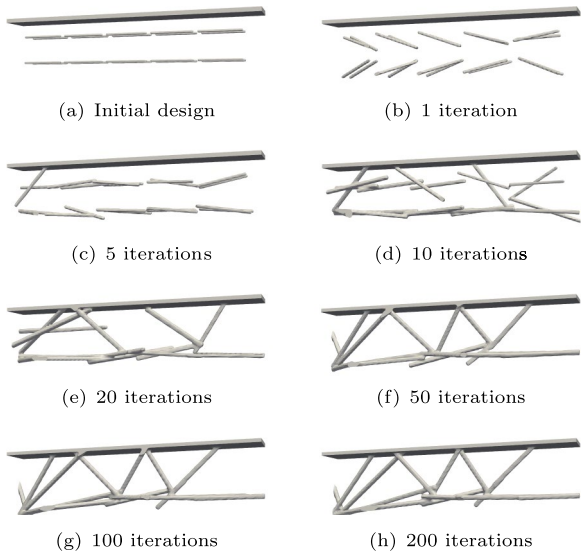

Fig. 16 Design iterates for 3D-bridge optimization with circular-tube section

q_2, q_3, t_x, t_y, t_z, and α; the number of elements $n_x \times n_y \times n_z$ in each dimension; and the corresponding total number of elements in the mesh N_e. This table also includes the number of elements N_r needed if the real section were to be modeled with at least two finite elements across the smallest dimension of the section. This requirement, as noted in Sect. 1, is necessary to ensure sensitivities of the projected density are well-defined. As observed from the numbers in the table, the resulting mesh would require billions of elements, making the solution of the optimization problem highly impractical. This simple example demonstrates that by employing the equivalent-section approached proposed in this work, it is possible to design ultralight structures using an individual engineering workstation.

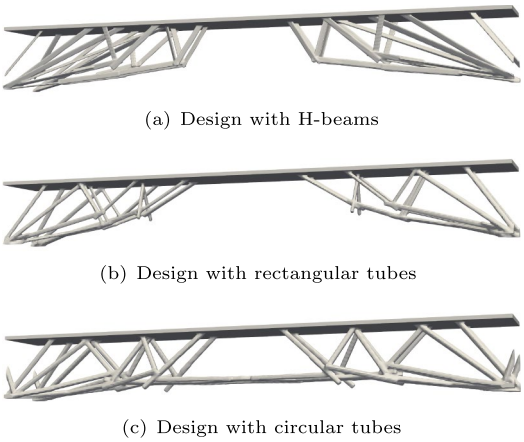

Fig. 17 3D-bridge optimization for the three different structural sections considered. The optimal design is reflected about the symmetry planes to show the entire bridge

Table 7 Summary of the 3D-bridge optimization for 0.2% of steel

3D bridge optimization			
Property	H-beam	Rectangular tube	Circular tube
$r*_c$(mm)	50	50	50
a(mm)	157.371	157.371	131.145
b(mm)	87.374	168.820	262.29
L_c(mm)	[1100, 7500]	[1000, 7500]	[1100, 7500]
q_0	$[-1, 1]$	$[-1, 1]$	$[-1, 1]$
q_1	$[-1, 1]$	$[-1, 1]$	$[-1, 1]$
q_2	$[-1, 1]$	$[-1, 1]$	$[-1, 1]$
q_3	$[-1, 1]$	$[-1, 1]$	$[-1, 1]$
t_x(mm)	[0, 1400]	[0, 1400]	[0, 1400]
t_y(mm)	[0, 3500]	[0, 3500]	[0, 3500]
t_z(mm)	[0, 1750]	[0, 1750]	[0, 1750]
α	[0, 1]	[0, 1]	[0, 1]
$\bar{v}_{eq}$	7.426%	7.473%	9.81%
N_e	1102736	432000	250000
$n_x \times n_y \times n_z$	$320 \times 40 \times 80$	$240 \times 30 \times 60$	$200 \times 25 \times 50$
N_r	3.340×10^9	1.340×10^9	5.488×10^9
N_{ite}	161	232	300
t_{ite} (s)	383.16	112.28	67.17
t_{total} (s)	116184.43	34104.96	20380.64
$\mathcal{C}$ (J)	353.14	354.36	360.54

7 Conclusion

This work formulated a novel method for the topology optimization of ultralight frame structures using structural shapes. The key ingredient of the proposed approach is to replace the geometric representation of a structural shape with an equivalent cross-section that has the same effective axial and bending stiffness. The fact that the equivalent section is larger than the corresponding original shape substantially decreases the number of elements required in the finite element analysis to perform the optimization. The proposed method also introduced an overlap constraint using auxiliary primitives that ensures that structural members do not intersect in ways that cannot be practically fabricated.

The computational design examples demonstrate the effectiveness of the proposed method in obtaining good designs that satisfy all the constraints, and show the method converges well within a reasonable number of iterations. The 3D-bridge example demonstrates the design of an ultralight structure ($\bar{v} = 0.2\%$) attained with a single engineering workstation. While computationally more expensive, the proposed method has important advantages when compared to ground-structure methods that employ 1D elements for the analysis. These advantages include the ability to produce good designs with only a few structural elements as the connectivity of the structure is not restricted to a subset of a ground structure. Also, the proposed method can capture 2D and 3D overlaps that cannot easily be modeled with 1D elements. Finally, although not studied in this work, the proposed method could in principle incorporate stress constraints that capture the stresses arising from the intersection of primitives as in, for example, Zhang et al. (2017); however, a correction would be needed to account for the equivalent sections.

The proposed methodology can be easily extended in multiple ways. It can be applied to structural shapes other than the ones studied in this work, including designs with asymmetric cross-sections like C- or T-sections. It could incorporate other structural criteria such as stresses, buckling, or vibrations. Finally, the structural shapes could be made of a reinforced material like a carbon-fiber-reinforced polymer, as in Smith and Norato (2021); a composite material with different properties in tension and compression such as reinforced concrete or a steel-concrete composite; or an anisotropic material like wood.

Other considerations to be addressed in future work include the incorporation of manufacturing cost considerations as in Gu et al. (2023), the design of structures made of multiple shapes, and the simultaneous optimization of the structural layout and the cross-sections.

Acknowledgements The first and last author thank the United States National Science Foundation, Award CMMI-1751211, for support of this work.

Declarations

Conflict of interest The authors declare that they have no Conflict of interest.

Replication of results The manuscript providesall the details of the formulation and all the datanecessary to replicate the results presented in theexamples. Relevant portions of the code and thedata pertaining the optimal designs in the presentedexamples can be shared upon reasonable request bycontacting the corresponding author.

References

Bates W, Association BCS (1987) Historical Structural Steelwork Handbook: Properties of U.K. and European Cast Iron, Wrought Iron and Steel Sections Including Design, Load and Stress Data Since the Mid 19th Century. Publication /BCSA. British Constructional Steelwork Association, London

Bendsøe MP, Ben-Tal A, Zowe J (1994) Optimization methods for truss geometry and topology design. Struct Optim 7:141–159

Bendsøe: Topology design of truss structures, pp. 221–259. Springer, Berlin, Heidelberg (2004)

Bendsøe M, Haber R (1993) The michell layout problem as a low volume fraction limit of the perforated plate topology optimization problem: an asymptotic study. Struct Optim 6:263–267

Bai J, Zuo W (2020) Hollow structural design in topology optimization via moving morphable component method. Struct Multidiscip Optim 61(1):187–205

Chandrasekhar A (2023) Polyto: Structural topology optimization using convex polygons. arXiv preprint arXiv:2305.04406

Changizi N, Jalalpour M (2017) Stress-based topology optimization of steel-frame structures using members with standard cross sections: Gradient-based approach. J Struct Eng 143(8):04017078

Guest JK, Asadpoure A, Ha S-H (2011) Eliminating beta-continuation from heaviside projection and density filter algorithms. Struct Multidiscip Optim 44:443–453

Gu H, Smith H, Norato JA (2023) Manufacturing-cost-driven topology optimization of welded frame structures. J Mech Des 145(8):081702

Hibbeler RC, Yap KB (2022) Mechanics of Materials, 11th edn. Pearson, Boston

Kuipers JB (2020) Quaternions and rotation sequences: a primer with applications to orbits. Aerospace and Virtual Reality. Princeton University Press, New Jersey

Kazemi H, Vaziri A, Norato JA (2020) Multi-material topology optimization of lattice structures using geometry projection. Comp Methods Appl Mech Eng 363:112895

Li B, Huang C, Xuan C, Liu X (2019) Dynamic stiffness design of plate/shell structures using explicit topology optimization. Thin-Walled Struct 140:542–564

Li L, Liu C, Zhang W, Du Z, Guo X (2021) Combined model-based topology optimization of stiffened plate structures via mmc approach. Int J Mech Sci 208:106682

Norato JA, Bell BK, Tortorelli DA (2015) A geometry projection method for continuum-based topology optimization with discrete elements. Comp Methods Appl Mech Eng 293:306–327

Norato JA (2018) Topology optimization with supershapes. Struct Multidiscip Optim 58(2):415–434

Norato JA, Smith HA, Deaton JD, Kolonay RM (2022) A maximum-rectifier-function approach to stress-constrained topology optimization. Struct Multidiscip Optim 65(10):286

Öchsner A (2021) Euler–Bernoulli Beam Theory, pp. 7–66. Springer, Cham (2021)

Rozvany GI (2011) A review of new fundamental principles in exact topology optimization. CMM-2011 Computer Methods in Mechanics

Shapiro V (2002) Solid modeling. Handbook of Comp Aided Geo Des 20:473–518

Savine F, Irisarri F-X, Julien C, Vincenti A, Guerin Y (2021) A component-based method for the optimization of stiffener layout on large cylindrical rib-stiffened shell structures. Struct Multidiscip Optim 64(4):1843–1861

Sigmund O, Maute K (2013) Topology optimization approaches: a comparative review. Struct Multidiscip Optim 48(6):1031–1055

Smith HA, Norato JA (2019) Geometric constraints for the topology optimization of structures made of primitives. SAMPE 2019-Charlotte, NC, May 2019

Smith H, Norato JA (2020) A MATLAB code for topology optimization using the geometry projection method. Struct Multidiscip Optim 62(3):1579–1594

Smith H, Norato JA (2021) Topology optimization with discrete geometric components made of composite materials. Comp Methods Appl Mech Eng 376:113582

Smith H, Norato J (2022) Topology optimization of structures made of fiber-reinforced plates. Struct Multidiscip Optim 65(2):58

Smith H, Norato J (2022) Topology optimization of structures made of fiber-reinforced plates. Struct Multidiscip Optim 65:58

Svanberg K (1987) The method of moving asymptotes-a new method for structural optimization. Int J Num Methods Eng 24(2):359–373

Wein F, Dunning PD, Norato JA (2020) A review on feature-mapping methods for structural optimization. Struct Multidiscip Optim 62(4):1597–1638

Wang J, Gao T, Zhu J, Zhang W (2024) Topology optimization with beam features of variable cross-sections. Struct Multidiscip Optim 67(6):96

Zhang S, Gain AL, Norato JA (2017) Stress-based topology optimization with discrete geometric components. Comp Methods Appl Mech Eng 325:1–21

Zhang S, Gain AL, Norato JA (2018) A geometry projection method for the topology optimization of curved plate structures with placement bounds. Int J Num Methods Eng 114(2):128–146

Zhao Y, Hoang V-N, Jang G-W, Zuo W (2021) Hollow structural topology optimization to improve manufacturability using three-dimensional moving morphable bars. Adv Eng Softw 152:102955

Zhang S, Norato JA, Gain AL, Lyu N (2016) A geometry projection method for the topology optimization of plate structures. Struct Multidiscip Optim 54(5):1173–1190

Zegard T, Paulino GH (2014) Grand-ground structure based topology optimization for arbitrary 2d domains using matlab. Struct Multidiscip Optim 50:861–882

Zhang W, Zhou L (2018) Topology optimization of self-supporting structures with polygon features for additive manufacturing. Comp Methods Appl Mech Eng 334:56–78